Three-Dimensional Wave-Field Simulation in Heterogeneous Transversely Isotropic Medium with Irregular Free Surface

by Haiqiang Lan and Zhongjie Zhang

Abstract Modeling of seismic-wave propagation in anisotropic medium with irregular topography is beneficial to interpret seismic data acquired by active and passive source seismology conducted in areas of interest such as mountain ranges and basins. The major challenge in this context is the difficulty in tackling the irregular free-surface boundary condition in a Cartesian coordinate system. To implement surface topography, we use the boundary-conforming grid and map a rectangular grid onto a curved grid. We use a stable and explicit second-order accurate finite-difference scheme to discretize the elastic wave equations (in a curvilinear coordinate system) in a 3D heterogeneous transversely isotropic medium. The free-surface boundary conditions are accurately applied by introducing a discretization that uses boundary-modified difference operators for the mixed derivatives in the governing equations. The accuracy of the proposed method is checked by comparing the numerical results obtained by the trial algorithm with the analytical solutions of the Lamb's problem, for an isotropic medium and a transversely isotropic medium with a vertical symmetry axis, respectively. Efficiency tests performed by different numerical experiments illustrate clearly the influence of an irregular (nonflat) free surface on seismic-wave propagation.

Introduction

Rough topography is very common and we have to deal with it during the acquisition, processing, and interpretation of seismic data. For example, in the context of the deep seismic soundings to explore the crustal structure, seismic experiments are usually carried out across: (1) orogenic belts for understanding the mechanisms; (2) basins to understand the formation mechanisms; and (3) transition zones for the study of its interaction (Boore, 1972; Jih *et al.*, 1988; Levander, 1990; Al-Shukri *et al.*, 1995; Robertsson, 1996; Ashford *et al.*, 1997; Robertsson and Holliger, 1997; Zhang and Klemperer, 2010; Zhang *et al.*, 2010). In oil/gas seismic exploration, seismologists also have a similar problem with the undulating topography along the survey line.

In the last two decades, several approaches have been proposed to simulate wave propagation in heterogeneous medium with irregular topography. These schemes include the finite-element method (Rial *et al.*, 1992; Toshinawa and Ohmachi, 1992); the spectral element method (Komatitsch and Vilotte, 1998; Komatitsch and Tromp, 1999, 2002); the pseudospectral method (Tessmer *et al.*, 1992; Tessmer and Kosloff, 1994; Nielsen *et al.*, 1994); the boundary element method (Campillo and Bouchon, 1985; Sánchez-Sesma *et al.*, 1985; Campillo, 1987; Bouchon *et al.*, 1989; Sánchez-Sesma and Campillo, 1991, 1993; Durand *et al.*, 1999; Liu and Zhang, 2001; Sánchez-Sesma *et al.*, 1993; Liu *et al.*, 2008); the finite-difference method (Wong, 1982; Jih *et al.*,

1988; Frankel and Vidale, 1992; Frankel, 1993; Hestholm and Ruud, 1994; Robertsson, 1996; Robertsson and Holliger, 1997; Hestholm and Ruud, 1998; Hestholm *et al.*, 1999; Oprsal and Zahradnik, 1999; Hayashi *et al.*, 2001; Hestholm, 2003; Gao and Zhang, 2006; W. Zhang and X. Chen, 2006; Lombard *et al.*, 2008), and also a hybrid approach that combines the staggered-grid finite-difference scheme with the finite-element method (Moczo *et al.*, 1997; Galis *et al.*, 2008). Both the spectral element and the finite-element methods satisfy boundary conditions on the free surface naturally. Three-dimensional surface and interface topographies can be modeled using curved piecewise elements. However, the classical finite-element method suffers from a high computational cost, and, on the other hand, a smaller spectral element than the one required by numerical dispersion is required to describe a highly curved topography, as demonstrated in seismic modeling of a hemispherical crater (Komatitsch and Tromp, 1999). The pseudospectral method is limited to a free surface with smoothly varying topography and leads to inaccuracies for models with strong heterogeneity or sharp boundaries (Tessmer *et al.*, 1992). The boundary integral equation and boundary element methods are not suitable for near-surface regions with large velocity contrasts (Bouchon *et al.*, 1995). The finite-difference method is one of the most popular numerical methods used in computational seismology. In comparison with other methods, the finite-difference method

is simpler and more flexible, although it has some difficulty in dealing with surface topography. The situation has improved recently. For rectangular domains, a stable and explicit discretization of the free-surface boundary conditions has been presented by Nilsson *et al.* (2007). By using boundary-modified difference operators, Nilsson *et al.* (2007) introduce a discretization of the mixed derivatives in the governing equations; they also show that the method is second-order accurate for problems with smoothly varying material properties and stable under standard Courant-Friedrichs-Lewy constraints, for arbitrarily varying material properties. Subsequently, Appelo and Petersson (2009) have generalized the results of Nilsson *et al.* (2007) to curvilinear coordinate systems, allowing for simulations on nonrectangular domains. They construct a stable discretization of the free-surface boundary conditions on curvilinear grids, and they prove that the strengths of the proposed method are its ease of implementation, efficiency (relative to low-order unstructured grid methods), geometric flexibility, and, most importantly, the bulletproof stability (Appelo and Petersson, 2009), even though they deal with 2D isotropic medium.

Nevertheless, the earth is often seismically anisotropic resulting from fractured rocks, fluid-filled cracks (Hudson, 1981; Crampin, 1981, 1984; Schoenberg and Muir, 1989; Liu *et al.*, 1993; Hsu and Schoenberg, 1993; Zhang *et al.*, 1999, 2000), thin isotropic layering (Backus, 1962; Helbig, 1984), lack of and homogeneity (Grechka and McMechan, 1995), or even preferential orientation of olivine (Forsyth, 1975; Dziewonski and Anderson, 1981). In this study, we follow the approach proposed by Appelo and Petersson (2009) and extend it to the 3D case with the purpose of simulating seismic-wave propagation in 3D heterogeneous anisotropic medium with nonflat surface topography. The paper is organized as follows: first, we briefly describe the boundary-conforming grid and the transformation between curvilinear coordinates and Cartesian coordinates; then we write the wave equations and free boundary conditions in these two coordinate systems; after that we introduce a numerical method to discretize both the wave equations and the free-surface boundary conditions. Finally, we present several numerical examples to demonstrate the accuracy and efficiency of the method.

Transformation between Curvilinear and Cartesian Coordinates

As to the topographic surface, the discrete grid must conform to the free surface to suppress artificial scattered waves. Such a grid is called the boundary-conforming grid (Thompson *et al.*, 1985; Hvid, 1994); it was used early by Fornberg (1988) in seismic-wave simulation with the pseudospectral method. A grid of this type is achieved by carrying out a transformation between the (curvilinear) computational space and the (Cartesian) physical space as illustrated in Figure 1. By means of this transformation, the curvilinear coordinates q, r, and s are mapped into Cartesian coordinates within the physical space, where both systems have positive direction
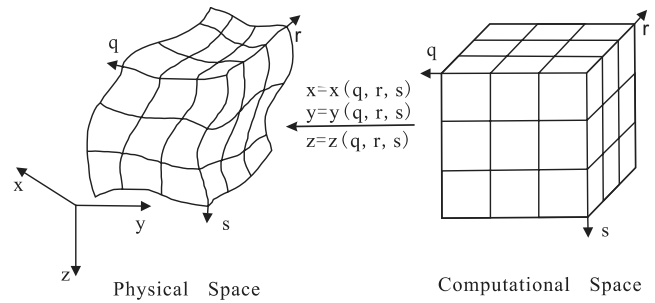

Figure 1. Mapping between computational and physical space in three dimensions (after Hvid, 1994).

downward for the vertical coordinate. A boundary in the physical space presents a constant value of one of the curvilinear coordinates, be it a curve in two dimensions or a surface in three dimensions.

Boundary-conforming grids may be of two fundamentally different types: structured and unstructured (or irregular) grids. A structured grid (Fig. 1) is characterized by having a fixed number of elements along each of the coordinate directions. The general element is a hexahedron in 3D, just as in the left panel of Figure 1. Neighboring elements in the physical space are also adjacent in the computational space, which is one of the great advantages of this type of grid. This property makes it relatively simple to implement in a computer. Structured grids are mainly used in finite difference and finite volume solvers. In this paper we focus on structured boundary-conforming grids. Several methods may be used to generate these grids, namely: Partial Differential Equation (PDE) methods, algebraic methods, co-normal mapping methods, and variational methods. Here we use PDE methods (see Thompson *et al.*, 1985 and Hvid, 1994 for details).

After generating the boundary-conforming grid, the Cartesian coordinates of every grid point can be determined from the curvilinear coordinates through the equation

$$x = x(q, r, s), \tag{1a}$$

$$y = y(q, r, s), \tag{1b}$$

$$z = z(q, r, s), \tag{1c}$$

then, we can express the spatial derivatives in the Cartesian coordinate system (x, y, z) from the curvilinear coordinate system (q, r, s) following the chain rule

$$\partial_x = q_x \partial_q + r_x \partial_r + s_x \partial_s, \tag{2a}$$

$$\partial_y = q_y \partial_q + r_y \partial_r + s_y \partial_s, \tag{2b}$$

$$\partial_z = q_z \partial_q + r_z \partial_r + s_z \partial_s, \tag{2c}$$

and similarly in other cases

$$\partial_q = x_q\partial_x + y_q\partial_y + z_q\partial_z, \tag{3a}$$

$$\partial_r = x_r\partial_x + y_r\partial_y + z_r\partial_z, \tag{3b}$$

$$\partial_s = x_s\partial_x + y_s\partial_y + z_s\partial_z, \tag{3c}$$

where q_x denotes $\partial q(x, y, z)/\partial x$ and the similar in other cases. These derivatives are called metric derivatives or simply the metric. We can also find the metric derivatives

$$q_x = \frac{1}{J}(y_r z_s - z_r y_s), \tag{4a}$$

$$q_y = \frac{1}{J}(z_r x_s - x_r z_s), \tag{4b}$$

$$q_z = \frac{1}{J}(x_r y_s - y_r x_s), \tag{4c}$$

$$r_x = \frac{1}{J}(y_s z_q - z_s y_q), \tag{4d}$$

$$r_y = \frac{1}{J}(z_s x_q - x_s z_q), \tag{4e}$$

$$r_z = \frac{1}{J}(x_s y_q - y_s x_q), \tag{4f}$$

$$s_x = \frac{1}{J}(y_q z_r - z_q y_r), \tag{4g}$$

$$s_y = \frac{1}{J}(z_q x_r - x_q z_r), \tag{4h}$$

$$s_z = \frac{1}{J}(x_q y_r - y_q x_r), \tag{4i}$$

where J is the Jacobian of the transformation that is written as

$$\begin{aligned} J = &\, x_q y_r z_s - x_q y_s z_r - x_r y_q z_s \\ &+ x_r y_s z_q + x_s y_q z_r - x_s y_r z_q, \end{aligned}$$

and whose detailed form can be found in Appendix A.

It is worth noting that even if the mapping equation (1) is given by an analytic function, the derivatives should still be calculated numerically to avoid spurious source terms due to the coefficients of the derivatives when the conservation form of the momentum equations are used (Thompson *et al.*, 1985). In all examples presented in this paper the metric derivatives are computed numerically using second-order accurate finite-difference approximations.

Elastic Wave Equations in Cartesian and Curvilinear Coordinate Systems

In the following paragraphs we consider a well-studied type of anisotropy in seismology, namely, a transversely isotropic medium. In the absence of external force, the elastic wave equations in the Cartesian coordinates are given by

$$\begin{aligned} \rho\frac{\partial^2 u}{\partial t^2} = &\, \frac{\partial}{\partial x}\left(c_{11}\frac{\partial u}{\partial x} + c_{12}\frac{\partial v}{\partial y} + c_{13}\frac{\partial w}{\partial z}\right) + \frac{\partial}{\partial y}\left(c_{66}\frac{\partial u}{\partial y}\right. \\ &\left. + c_{66}\frac{\partial v}{\partial x}\right) + \frac{\partial}{\partial z}\left(c_{44}\frac{\partial u}{\partial z} + c_{44}\frac{\partial w}{\partial x}\right), \end{aligned} \tag{5a}$$

$$\begin{aligned} \rho\frac{\partial^2 v}{\partial t^2} = &\, \frac{\partial}{\partial x}\left(c_{66}\frac{\partial v}{\partial x} + c_{66}\frac{\partial u}{\partial y}\right) + \frac{\partial}{\partial y}\left(c_{11}\frac{\partial v}{\partial y} + c_{12}\frac{\partial u}{\partial x}\right. \\ &\left. + c_{13}\frac{\partial w}{\partial z}\right) + \frac{\partial}{\partial z}\left(c_{44}\frac{\partial v}{\partial z} + c_{44}\frac{\partial w}{\partial y}\right), \end{aligned} \tag{5b}$$

$$\begin{aligned} \rho\frac{\partial^2 w}{\partial t^2} = &\, \frac{\partial}{\partial x}\left(c_{44}\frac{\partial w}{\partial x} + c_{44}\frac{\partial u}{\partial z}\right) + \frac{\partial}{\partial y}\left(c_{44}\frac{\partial w}{\partial y} + c_{44}\frac{\partial v}{\partial z}\right) \\ &+ \frac{\partial}{\partial z}\left(c_{33}\frac{\partial w}{\partial z} + c_{13}\frac{\partial u}{\partial x} + c_{13}\frac{\partial v}{\partial y}\right), \end{aligned} \tag{5c}$$

where $c_{ij}(x, y, z)$ are elastic parameters and $c_{66} = 0.5(c_{11} - c_{12})$; u, v, and w are the displacements in x, y, and z directions, respectively; $\rho(x, y, z)$ is density. Equations (5a)–(5c) are complemented by the initial data

$$u(x, y, z, 0) = u_0(x, y, z), \tag{6a}$$

$$v(x, y, z, 0) = v_0(x, y, z), \tag{6b}$$

$$w(x, y, z, 0) = w_0(x, y, z), \tag{6c}$$

$$\frac{\partial u(x, y, z, 0)}{\partial t} = u_1(x, y, z), \tag{6d}$$

$$\frac{\partial v(x, y, z, 0)}{\partial t} = v_1(x, y, z), \tag{6e}$$

$$\frac{\partial w(x, y, z, 0)}{\partial t} = w_1(x, y, z). \tag{6f}$$

Utilizing relationships (2a)–(2c), the wave equations (5a)–(5c) can be rewritten in the curvilinear coordinate system in the following form (see Appendix B for details):

$$J\rho\frac{\partial^2 u}{\partial t^2} = \frac{\partial}{\partial q}\{Jq_x[c_{11}(q_x\partial_q + r_x\partial_r + s_x\partial_s)u + c_{12}(q_y\partial_q + r_y\partial_r + s_y\partial_s)v + c_{13}(q_z\partial_q + r_z\partial_r + s_z\partial_s)w]$$

$$+ Jq_y[c_{66}(q_x\partial_q + r_x\partial_r + s_x\partial_s)v + c_{66}(q_y\partial_q + r_y\partial_r + s_y\partial_s)u]$$

$$+ Jq_z[c_{44}(q_z\partial_q + r_z\partial_r + s_z\partial_s)u + c_{44}(q_x\partial_q + r_x\partial_r + s_x\partial_s)w]\}$$

$$+ \frac{\partial}{\partial r}\{Jr_x[c_{11}(q_x\partial_q + r_x\partial_r + s_x\partial_s)u + c_{12}(q_y\partial_q + r_y\partial_r + s_y\partial_s)v + c_{13}(q_z\partial_q + r_z\partial_r + s_z\partial_s)w]$$

$$+ Jr_y[c_{66}(q_x\partial_q + r_x\partial_r + s_x\partial_s)v + c_{66}(q_y\partial_q + r_y\partial_r + s_y\partial_s)u]$$

$$+ Jr_z[c_{44}(q_z\partial_q + r_z\partial_r + s_z\partial_s)u + c_{44}(q_x\partial_q + r_x\partial_r + s_x\partial_s)w]\}$$

$$+ \frac{\partial}{\partial s}\{Js_x[c_{11}(q_x\partial_q + r_x\partial_r + s_x\partial_s)u + c_{12}(q_y\partial_q + r_y\partial_r + s_y\partial_s)v + c_{13}(q_z\partial_q + r_z\partial_r + s_z\partial_s)w]$$

$$+ Js_y[c_{66}(q_x\partial_q + r_x\partial_r + s_x\partial_s)v + c_{66}(q_y\partial_q + r_y\partial_r + s_y\partial_s)u]$$

$$+ Js_z[c_{44}(q_z\partial_q + r_z\partial_r + s_z\partial_s)u + c_{44}(q_x\partial_q + r_x\partial_r + s_x\partial_s)w]\}, \tag{7}$$

$$J\rho\frac{\partial^2 v}{\partial t^2} = \frac{\partial}{\partial q}\{Jq_x[c_{66}(q_x\partial_q + r_x\partial_r + s_x\partial_s)v + c_{66}(q_y\partial_q + r_y\partial_r + s_y\partial_s)u]$$

$$+ Jq_y[c_{11}(q_y\partial_q + r_y\partial_r + s_y\partial_s)v + c_{12}(q_x\partial_q + r_x\partial_r + s_x\partial_s)u + c_{13}(q_z\partial_q + r_z\partial_r + s_z\partial_s)w]$$

$$+ Jq_z[c_{44}(q_z\partial_q + r_z\partial_r + s_z\partial_s)v + c_{44}(q_y\partial_q + r_y\partial_r + s_y\partial_s)w]\}$$

$$+ \frac{\partial}{\partial r}\{Jr_x[c_{66}(q_x\partial_q + r_x\partial_r + s_x\partial_s)v + c_{66}(q_y\partial_q + r_y\partial_r + s_y\partial_s)u]$$

$$+ Jr_y[c_{11}(q_y\partial_q + r_y\partial_r + s_y\partial_s)v + c_{12}(q_x\partial_q + r_x\partial_r + s_x\partial_s)u + c_{13}(q_z\partial_q + r_z\partial_r + s_z\partial_s)w]$$

$$+ Jr_z[c_{44}(q_z\partial_q + r_z\partial_r + s_z\partial_s)v + c_{44}(q_y\partial_q + r_y\partial_r + s_y\partial_s)w]\}$$

$$+ \frac{\partial}{\partial s}\{Js_x[c_{66}(q_x\partial_q + r_x\partial_r + s_x\partial_s)v + c_{66}(q_y\partial_q + r_y\partial_r + s_y\partial_s)u]$$

$$+ Js_y[c_{11}(q_y\partial_q + r_y\partial_r + s_y\partial_s)v + c_{12}(q_x\partial_q + r_x\partial_r + s_x\partial_s)u + c_{13}(q_z\partial_q + r_z\partial_r + s_z\partial_s)w]$$

$$+ Js_z[c_{44}(q_z\partial_q + r_z\partial_r + s_z\partial_s)v + c_{44}(q_y\partial_q + r_y\partial_r + s_y\partial_s)w]\}, \tag{8}$$

$$J\rho\frac{\partial^2 w}{\partial t^2} = \frac{\partial}{\partial q}\{Jq_x[c_{44}(q_z\partial_q + r_z\partial_r + s_z\partial_s)u + c_{44}(q_x\partial_q + r_x\partial_r + s_x\partial_s)w]$$

$$+ Jq_y[c_{44}(q_z\partial_q + r_z\partial_r + s_z\partial_s)v + c_{44}(q_y\partial_q + r_y\partial_r + s_y\partial_s)w]$$

$$+ Jq_z[c_{33}(q_z\partial_q + r_z\partial_r + s_z\partial_s)w + c_{13}(q_x\partial_q + r_x\partial_r + s_x\partial_s)u + c_{13}(q_y\partial_q + r_y\partial_r + s_y\partial_s)v]\}$$

$$+ \frac{\partial}{\partial r}\{Jr_x[c_{44}(q_z\partial_q + r_z\partial_r + s_z\partial_s)u + c_{44}(q_x\partial_q + r_x\partial_r + s_x\partial_s)w]$$

$$+ Jr_y[c_{44}(q_z\partial_q + r_z\partial_r + s_z\partial_s)v + c_{44}(q_y\partial_q + r_y\partial_r + s_y\partial_s)w]$$

$$+ Jr_z[c_{33}(q_z\partial_q + r_z\partial_r + s_z\partial_s)w + c_{13}(q_x\partial_q + r_x\partial_r + s_x\partial_s)u + c_{13}(q_y\partial_q + r_y\partial_r + s_y\partial_s)v]\}$$

$$+ \frac{\partial}{\partial s}\{Js_x[c_{44}(q_z\partial_q + r_z\partial_r + s_z\partial_s)u + c_{44}(q_x\partial_q + r_x\partial_r + s_x\partial_s)w]$$

$$+ Js_y[c_{44}(q_z\partial_q + r_z\partial_r + s_z\partial_s)v + c_{44}(q_y\partial_q + r_y\partial_r + s_y\partial_s)w]$$

$$+ Js_z[c_{33}(q_z\partial_q + r_z\partial_r + s_z\partial_s)w + c_{13}(q_x\partial_q + r_x\partial_r + s_x\partial_s)u + c_{13}(q_y\partial_q + r_y\partial_r + s_y\partial_s)v]\}. \tag{9}$$

Free Boundary Conditions in the Cartesian and Curvilinear Coordinate Systems

At the free surface, the boundary conditions in the Cartesian coordinates are given by

$$\begin{bmatrix} c_{11}\frac{\partial u}{\partial x} + c_{12}\frac{\partial v}{\partial y} + c_{13}\frac{\partial w}{\partial z} & c_{66}\frac{\partial u}{\partial y} + c_{66}\frac{\partial v}{\partial x} & c_{44}\frac{\partial u}{\partial z} + c_{44}\frac{\partial w}{\partial x} \\ c_{66}\frac{\partial v}{\partial x} + c_{66}\frac{\partial u}{\partial y} & c_{11}\frac{\partial v}{\partial y} + c_{12}\frac{\partial u}{\partial x} + c_{13}\frac{\partial w}{\partial z} & c_{44}\frac{\partial v}{\partial z} + c_{44}\frac{\partial w}{\partial y} \\ c_{44}\frac{\partial w}{\partial x} + c_{44}\frac{\partial u}{\partial z} & c_{44}\frac{\partial w}{\partial y} + c_{44}\frac{\partial v}{\partial z} & c_{33}\frac{\partial w}{\partial z} + c_{13}\frac{\partial u}{\partial x} + c_{13}\frac{\partial v}{\partial y} \end{bmatrix} \begin{bmatrix} n_x \\ n_y \\ n_z \end{bmatrix} = 0. \tag{10}$$

Here $[n_x, n_y, n_z]^T$ is the inward normal of the free surface. Using relationships (2a)–(2c), the boundary conditions in the curvilinear coordinates of equation (10) can be rewritten as

$$\bar{s}_x c_{11}(q_x u_q + r_x u_r + s_x u_s) + c_{12}(q_y v_q + r_y v_r + s_y v_s)$$
$$+ c_{13}(q_z w_q + r_z w_r + s_z w_s)]$$
$$+ \bar{s}_y[c_{66}(q_y u_q + r_y u_r + s_y u_s)$$
$$+ c_{66}(q_x v_q + r_x v_r + s_x v_s)]$$
$$+ \bar{s}_z[c_{44}(q_z u_q + r_z u_r + s_z u_s)$$
$$+ c_{44}(q_x w_q + r_x w_r + s_x w_s)]$$
$$= 0, \tag{11}$$

$$\bar{s}_x[c_{66}(q_x v_q + r_x v_r + s_x v_s) + c_{66}(q_y u_q + r_y u_r + s_y u_s)]$$
$$+ \bar{s}_y[c_{11}(q_y v_q + r_y v_r + s_y v_s)$$
$$+ c_{12}(q_x u_q + r_x u_r + s_x u_s)$$
$$+ c_{13}(q_z w_q + r_z w_r + s_z w_s)]$$
$$+ \bar{s}_z[c_{44}(q_z v_q + r_z v_r + s_z v_s)$$
$$+ c_{44}(q_y w_q + r_y w_r + s_y w_s)]$$
$$= 0, \tag{12}$$

$$\bar{s}_x[c_{44}(q_x w_q + r_x w_r + s_x w_s) + c_{44}(q_z u_q + r_z u_r + s_z u_s)]$$
$$+ \bar{s}_y[c_{44}(q_y w_q + r_y w_r + s_y w_s)$$
$$+ c_{44}(q_z v_q + r_z v_r + s_z v_s)]$$
$$+ \bar{s}_z[c_{33}(q_z w_q + r_z w_r + s_z w_s)$$
$$+ c_{13}(q_x u_q + r_x u_r + s_x u_s)$$
$$+ c_{13}(q_y v_q + r_y v_r + s_y v_s)]$$
$$= 0. \tag{13}$$

Note that here the normal is represented by the normalized metric (evaluated along the free surface)

$$\bar{s}_x = \frac{s_x}{\sqrt{s_x^2 + s_y^2 + s_z^2}}, \qquad \bar{s}_y = \frac{s_y}{\sqrt{s_x^2 + s_y^2 + s_z^2}},$$

$$\bar{s}_z = \frac{s_z}{\sqrt{s_x^2 + s_y^2 + s_z^2}}.$$

A Discretization Scheme on the Curvilinear Grid

To approximate (7)–(9) we discretize the rectangular solid (Fig. 2)

$$q_i = (i-1)h_q, \quad i = 1, \dots, N_q, \quad h_q = l/(N_q - 1),$$
$$r_j = (j-1)h_r, \quad j = 1, \dots, N_r, \quad h_r = w/(N_r - 1),$$
$$s_k = (k-1)h_s, \quad k = 1, \dots, N_s, \quad h_s = h/(N_s - 1), \tag{14}$$

where l, w, and h are the length of the rectangular solid in q, r, and s directions, respectively; h_q, h_r, and $h_s > 0$ define the grid size in q, r, and s directions, respectively. The three components of the wave field are given by

$$[u_{i,j,k}(t), v_{i,j,k}(t), w_{i,j,k}(t)] = [u(q_i, r_j, s_k, t),$$
$$v(q_i, r_j, s_k, t), w(q_i, r_j, s_k, t)],$$

and the derivation operators are given as
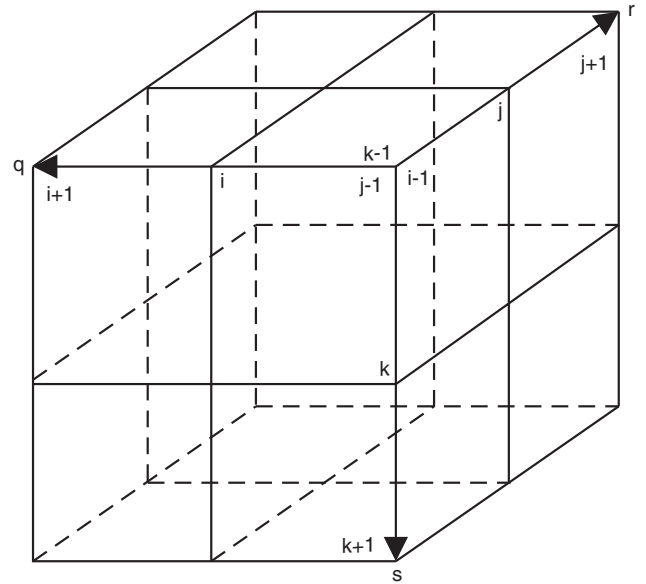
Figure 2. Grids distributions in curvilinear coordinate. The free surface is set to be at $k = 1$ layer, we use the forward difference (D_+^s) to approximate the normal derivative in the mixed derivatives on this layer; on other layers, the centered difference scheme (D_0^s) is used.

$$D_+^q u_{i,j,k} = \frac{u_{i+1,j,k} - u_{i,j,k}}{h_q}, \qquad D_-^q u_{i,j,k} = D_+^q u_{i-1,j,k},$$

$$D_0^q u_{i,j,k} = \frac{1}{2}(D_+^q u_{i,j,k} + D_-^q u_{i,j,k}),$$

$$D_+^r u_{i,j,k} = \frac{u_{i,j+1,k} - u_{i,j,k}}{h_r}, \qquad D_-^r u_{i,j,k} = D_+^r u_{i,j-1,k},$$

$$D_0^r u_{i,j,k} = \frac{1}{2}(D_+^r u_{i,j,k} + D_-^r u_{i,j,k}),$$

$$D_+^s u_{i,j,k} = \frac{u_{i,j,k+1} - u_{i,j,k}}{h_s}, \qquad D_-^s u_{i,j,k} = D_+^s u_{i,j,k-1},$$

$$D_0^s u_{i,j,k} = \frac{1}{2}(D_+^s u_{i,j,k} + D_-^s u_{i,j,k}). \tag{15}$$

The right-hand sides of equations (7)–(9) contain spatial derivatives of nine basic types, which are discretized according to the following equations

$$\frac{\partial}{\partial q}(a\omega_q) \approx D_-^q(E_{1/2}^q(a)D_+^q\omega),$$

$$\frac{\partial}{\partial q}(b\omega_r) \approx D_0^q(bD_0^r\omega), \qquad \frac{\partial}{\partial q}(c\omega_s) \approx D_0^q(c\tilde{D}_0^s\omega),$$

$$\frac{\partial}{\partial r}(d\omega_q) \approx D_0^r(dD_0^q\omega), \qquad \frac{\partial}{\partial r}(e\omega_r) \approx D_-^r(E_{1/2}^r(e)D_+^r\omega),$$

$$\frac{\partial}{\partial r}(f\omega_s) \approx D_0^r(f\tilde{D}_0^s\omega), \qquad \frac{\partial}{\partial s}(g\omega_q) \approx \tilde{D}_0^s(gD_0^q\omega),$$

$$\frac{\partial}{\partial s}(m\omega_r) \approx \tilde{D}_0^s(mD_0^r\omega),$$

$$\frac{\partial}{\partial s}(p\omega_s) \approx D_-^s(E_{1/2}^s(p)D_+^s\omega). \tag{16}$$

Here ω represents u, v, or w; a, b, c, d, e, f, g, m, and p are combinations of metric and material coefficients. We introduce the following averaging operators

$$E_{1/2}^q(\gamma_{i,j,k}) = \gamma_{i+1/2,j,k} = \frac{\gamma_{i,j,k} + \gamma_{i+1,j,k}}{2},$$

$$E_{1/2}^r(\gamma_{i,j,k}) = \gamma_{i,j+1/2,k} = \frac{\gamma_{i,j,k} + \gamma_{i,j+1,k}}{2},$$

$$E_{1/2}^s(\gamma_{i,j,k}) = \gamma_{i,j,k+1/2} = \frac{\gamma_{i,j,k} + \gamma_{i,j,k+1}}{2}. \tag{17}$$

The cross terms that contain a normal derivative on the boundary are discretized on one side in the direction normal to the boundary

$$\tilde{D}_0^s u_{i,j,k} = \begin{cases} D_+^s u_{i,j,k}, & k = 1, \\ D_0^s u_{i,j,k}, & k \geq 2. \end{cases} \tag{18}$$

A Discretization on the Curvilinear Grid: Elastic Wave Equations

We approximate the spatial operators in equations (7)–(9) by (16). After suppressing grid indexes, this leads to

$$\begin{aligned}
J\rho\frac{\partial^2 u}{\partial t^2} =& D_-^q[E_{1/2}^q(M_1^{qq})D_+^q u + E_{1/2}^q(M_2^{qq})D_+^q v + E_{1/2}^q(M_3^{qq})D_+^q w] + D_0^q[M_1^{qs}\tilde{D}_0^s u + M_2^{qs}\tilde{D}_0^s v + M_3^{qs}\tilde{D}_0^s w] \\
&+ D_0^r[M_1^{rs}\tilde{D}_0^s u + M_2^{rs}\tilde{D}_0^s v + M_3^{rs}\tilde{D}_0^s w] + \tilde{D}_0^s[M_1^{sq}D_0^q u + M_2^{sq}D_0^q v + M_3^{sq}D_0^q w] \\
&+ \tilde{D}_0^s[M_1^{sr}D_0^r u + M_2^{sr}D_0^r v + M_3^{sr}D_0^r w] + D_0^q[M_1^{qr}D_0^r u + M_2^{qr}D_0^r v + M_3^{qr}D_0^r w] \\
&+ D_0^r[M_1^{rq}D_0^q u + M_2^{rq}D_0^q v + M_3^{rq}D_0^q w] + D_-^r[E_{1/2}^r(M_1^{rr})D_+^r u + E_{1/2}^r(M_2^{rr})D_+^r v + E_{1/2}^r(M_3^{rr})D_+^r w] \\
&+ D_-^s[E_{1/2}^s(M_1^{ss})D_+^s u + E_{1/2}^s(M_2^{ss})D_+^s v + E_{1/2}^s(M_3^{ss})D_+^s w] \equiv L^{(u)}(u,v,w),
\end{aligned} \tag{19}$$

$$\begin{aligned}
J\rho\frac{\partial^2 v}{\partial t^2} =& D_-^q[E_{1/2}^q(M_5^{qq})D_+^q v + E_{1/2}^q(M_2^{qq})D_+^q u + E_{1/2}^q(M_4^{qq})D_+^q w] + D_0^q[M_5^{qs}\tilde{D}_0^s v + M_2^{sq}\tilde{D}_0^s u + M_4^{qs}\tilde{D}_0^s w] \\
&+ D_0^r[M_5^{rs}\tilde{D}_0^s v + M_2^{sr}\tilde{D}_0^s u + M_4^{rs}\tilde{D}_0^s w] + \tilde{D}_0^s[M_5^{sq}D_0^q v + M_2^{qs}D_0^q u + M_4^{sq}D_0^q w] \\
&+ \tilde{D}_0^s[M_5^{sr}D_0^r v + M_2^{rs}D_0^r u + M_4^{sr}D_0^r w] + D_0^q[M_5^{qr}D_0^r v + M_2^{rq}D_0^r u + M_4^{qr}D_0^r w] \\
&+ D_0^r[M_5^{rq}D_0^q v + M_2^{qr}D_0^q u + M_4^{rq}D_0^q w] + D_-^r[E_{1/2}^r(M_5^{rr})D_+^r v + E_{1/2}^r(M_2^{rr})D_+^r u + E_{1/2}^r(M_4^{rr})D_+^r w] \\
&+ D_-^s[E_{1/2}^s(M_5^{ss})D_+^s v + E_{1/2}^s(M_2^{ss})D_+^s u + E_{1/2}^s(M_4^{ss})D_+^s w] \equiv L^{(v)}(u,v,w),
\end{aligned} \tag{20}$$

$$J\rho\frac{\partial^2 w}{\partial t^2} = D_-^q[E_{1/2}^q(M_3^{qq})D_+^q u + E_{1/2}^q(M_4^{qq})D_+^q v + E_{1/2}^q(M_6^{qq})D_+^q w] + D_0^q[M_3^{sq}\tilde{D}_0^s u + M_4^{sq}\tilde{D}_0^s v + M_6^{qs}\tilde{D}_0^s w]$$

$$+ D_0^r[M_3^{sr}\tilde{D}_0^s u + M_4^{sr}\tilde{D}_0^s v + M_6^{rs}\tilde{D}_0^s w] + \tilde{D}_0^s[M_3^{qs}D_0^q u + M_4^{qs}D_0^q v + M_6^{sq}D_0^q w]$$

$$+ \tilde{D}_0^s[M_3^{rs}D_0^r u + M_4^{rs}D_0^r v + M_6^{sr}D_0^r w] + D_0^q[M_3^{rq}D_0^r u + M_4^{rq}D_0^r v + M_6^{qr}D_0^r w]$$

$$+ D_0^r[M_3^{qr}D_0^q u + M_4^{qr}D_0^q v + M_6^{rq}D_0^q w] + D_-^r[E_{1/2}^r(M_3^{rr})D_+^r u + E_{1/2}^r(M_4^{rr})D_+^r v + E_{1/2}^r(M_6^{rr})D_+^r w]$$

$$+ D_-^s[E_{1/2}^s(M_3^{ss})D_+^s u + E_{1/2}^s(M_4^{ss})D_+^s v + E_{1/2}^s(M_6^{ss})D_+^s w] \equiv L^{(w)}(u,v,w), \tag{21}$$

in the grid points (q_i, r_j, s_k), $(i,j,k) \in [1, N_q] \times [1, N_r] \times [1, N_s]$. We have introduced the following notations for the material and metric terms in order to express the discretized equations in a more compact form:

$$M_1^{kl} = Jk_x l_x c_{11} + Jk_y l_y c_{66} + Jk_z l_z c_{44},$$

$$M_2^{kl} = Jk_x l_y c_{12} + Jk_y l_x c_{66},$$

$$M_3^{kl} = Jk_x l_z c_{13} + Jk_z l_x c_{44},$$

$$M_4^{kl} = Jk_y l_z c_{13} + Jk_z l_y c_{44},$$

$$M_5^{kl} = Jk_x l_x c_{66} + Jk_y l_y c_{11} + Jk_z l_z c_{44},$$

$$M_6^{kl} = Jk_x l_x c_{44} + Jk_y l_y c_{44} + Jk_z l_z c_{33}, \tag{22}$$

where k and l represent the metric coefficients q, r, or s.

We discretize in time using second-order accurate centered differences. The full set of discretized equations is

$$\rho\left(\frac{u^{n+1} - 2u^n + u^{n-1}}{\delta_t^2}\right) = L^{(u)}(u^n, v^n, w^n),$$

$$\rho\left(\frac{v^{n+1} - 2v^n + v^{n-1}}{\delta_t^2}\right) = L^{(v)}(u^n, v^n, w^n),$$

$$\rho\left(\frac{w^{n+1} - 2w^n + w^{n-1}}{\delta_t^2}\right) = L^{(w)}(u^n, v^n, w^n), \tag{23}$$

where δ_t represents the timestep.

A Discretization on the Curvilinear Grid: Free Boundary Conditions

The boundary conditions (11)–(13) are discretized by

$$\frac{1}{2}[(M_1^{ss})_{i,j,3/2}D_+^s u_{i,j,1} + (M_1^{ss})_{i,j,1/2}D_+^s u_{i,j,0}] + (M_1^{sq})_{i,j,1}D_0^q u_{i,j,1} + (M_2^{sq})_{i,j,1}D_0^q v_{i,j,1} + (M_3^{sq})_{i,j,1}D_0^q w_{i,j,1}$$

$$+ \frac{1}{2}[(M_2^{ss})_{i,j,3/2}D_+^s v_{i,j,1} + (M_2^{ss})_{i,j,1/2}D_+^s v_{i,j,0}] + (M_1^{sr})_{i,j,1}D_0^r u_{i,j,1} + (M_2^{sr})_{i,j,1}D_0^r v_{i,j,1} + (M_3^{sr})_{i,j,1}D_0^r w_{i,j,1}$$

$$+ \frac{1}{2}[(M_3^{ss})_{i,j,3/2}D_+^s w_{i,j,1} + (M_3^{ss})_{i,j,1/2}D_+^s w_{i,j,0}]$$

$$= 0, \tag{24}$$

$$\frac{1}{2}[(M_5^{ss})_{i,j,3/2}D_+^s v_{i,j,1} + (M_5^{ss})_{i,j,1/2}D_+^s v_{i,j,0}] + (M_5^{sq})_{i,j,1}D_0^q v_{i,j,1} + (M_2^{qs})_{i,j,1}D_0^q u_{i,j,1} + (M_4^{sq})_{i,j,1}D_0^q w_{i,j,1}$$

$$+ \frac{1}{2}[(M_2^{ss})_{i,j,3/2}D_+^s u_{i,j,1} + (M_2^{ss})_{i,j,1/2}D_+^s u_{i,j,0}] + (M_5^{sr})_{i,j,1}D_0^r v_{i,j,1} + (M_2^{rs})_{i,j,1}D_0^r u_{i,j,1} + (M_4^{sr})_{i,j,1}D_0^r w_{i,j,1}$$

$$+ \frac{1}{2}[(M_4^{ss})_{i,j,3/2}D_+^s w_{i,j,1} + (M_4^{ss})_{i,j,1/2}D_+^s w_{i,j,0}]$$

$$= 0, \tag{25}$$

$$\frac{1}{2}[(M_3^{ss})_{i,j,3/2}D_+^s u_{i,j,1} + (M_3^{ss})_{i,j,1/2}D_+^s u_{i,j,0}] + (M_3^{qs})_{i,j,1}D_0^q u_{i,j,1} + (M_4^{qs})_{i,j,1}D_0^q v_{i,j,1} + (M_6^{sq})_{i,j,1}D_0^q w_{i,j,1}$$

$$+ \frac{1}{2}[(M_4^{ss})_{i,j,3/2}D_+^s v_{i,j,1} + (M_4^{ss})_{i,j,1/2}D_+^s v_{i,j,0}] + (M_3^{rs})_{i,j,1}D_0^r u_{i,j,1} + (M_4^{rs})_{i,j,1}D_0^r v_{i,j,1} + (M_6^{sr})_{i,j,1}D_0^r w_{i,j,1}$$

$$+ \frac{1}{2}[(M_6^{ss})_{i,j,3/2}D_+^s w_{i,j,1} + (M_6^{ss})_{i,j,1/2}D_+^s w_{i,j,0}]$$

$$= 0, \tag{26}$$

for $i = 1, \ldots, N_q$; $j = 1, \ldots, N_r$.

The key step in obtaining a stable explicit discretization is to use the operator $\tilde{D}_0^s$ (which is one-sided on the boundary) for the approximation of the normal derivative in $\partial_q\partial_s$, $\partial_r\partial_s$, $\partial_s\partial_q$, and $\partial_s\partial_r$ cross derivatives. At first glance, it may appear that using a one-sided operator would reduce the accuracy of the method to the first order. However, as it was theoretically shown by Nilsson *et al.* (2007) (for a Cartesian discretization), a first-order error on the boundary in the differential equations (19)–(21) can be absorbed as a second-order perturbation of the boundary conditions (24)–(26).

In the finite-difference calculations, an artificial reflection arises at the edges of the model domain. To suppress this spurious reflection, we adopt a combined absorbing boundary condition by combing the *n*-time decoupled absorbing boundary condition (Zhang *et al.*, 1999; Yang *et al.*, 2002; Yang *et al.*, 2003) and exponential damping (Cerjan *et al.*, 1985). In this paper, we choose $n = 2$, and the detailed derivations and discretization can be found in the early papers due to Zhang *et al.* (1993), Yang (1996), and He and Zhang (1996).

Accuracy and Efficiency Tests

Accuracy

The accuracy of the proposed method is examined by comparing the numerical results with the analytical solution of the Lamb's problem, first in an isotropic medium and then in a transversely isotropic case with a vertical symmetry axis (VTI medium).

Analytic Comparison for the Lamb's Problem in an Isotropic Medium. We choose a half-infinite elastic medium where the *P* velocity is 623 m/s, the *S* velocity is 360 m/s, and the density is 1500 kg $\cdot$ m^{-3} (a Poisson solid). A vertical Ricker wavelet point source, with a center frequency of 2 Hz (containing frequencies up to 6 Hz), is loaded at a point 60 m below the surface. Thus, in the chosen model of medium, the dominant and minimum wavelengths of the *S* wave are $\lambda_{dom}^S = 180$ and $\lambda_{min}^S = 60$ m, respectively. The solutions with the grid spacings of 10 and 5 m, respectively, are benchmarked against an analytical solution by H. Zhang and X. Chen (2006). The numbers of grid points per shortest shear wavelength for both of these grid intervals are about 6 and 12, respectively. We present the time-series of the vertical component recorded 180, 1080, and 1980 m from the source, that is, records at the distances of 1, 6, and 11 times the dominant wavelength from the source, respectively (Fig. 3). It can be seen clearly that the results with 12 grid spacings per minimum wavelength (GSPMW) give much better agreements with the analytic solutions than those with only 6 GSPMW, and the former also give a sufficient accuracy in modeling Rayleigh wave propagation even for large distances.

In the following, we evaluate the accuracy of the numerical method in a quantitative way by using an error criterion defined by Kristek *et al.* (2002). The results are given in Figure 4. It can be clearly seen that the results with 12 GSPMW give much better amplitudes of Rayleigh waves than those with only 6 GSPMW, while both results give good phases. This is in agreement with the conclusion based on simple visual comparisons of the seismograms.

Analytic Comparison for the Lamb's Problem in a VTI Medium. The elastic parameters describing the VTI medium are given in Table 1. The analytical solution is obtained by convolving the free-surface Green's function with the source function (Payton, 1983; He and Zhang, 1996). A vertical point source of the type:
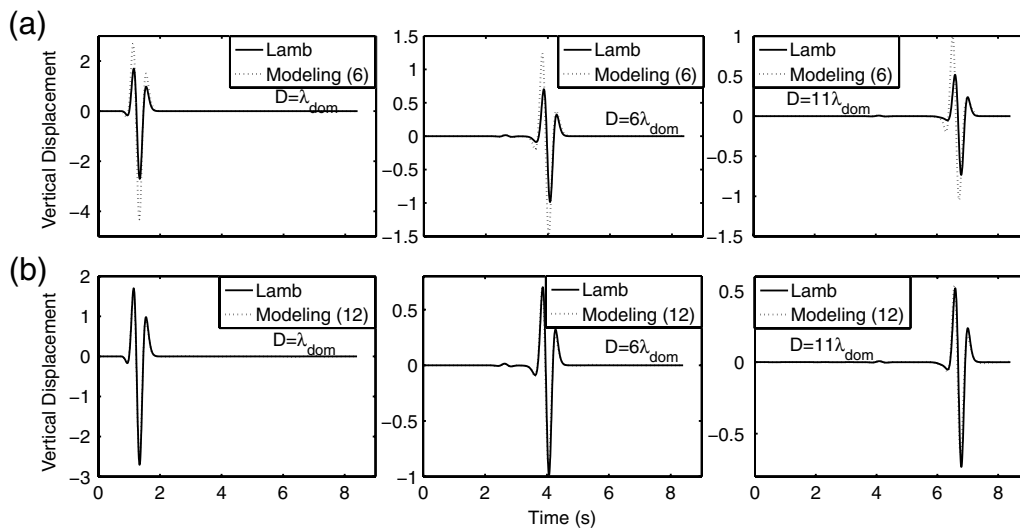
Figure 3. Comparison between numerical and analytical vertical components of the displacement at the epicentral distances of λ_{dom}^S, $6\lambda_{dom}^S$, and $11\lambda_{dom}^S$, respectively, for the Lamb's problem in the isotropic medium. Lamb's result is the analytical solution while the modeling result is the numerical solution. Numbers 6 and 12 mean the numbers of the grid spacings per minimum wavelength used in the numerical calculation.

Table 1

Medium Parameters in the Homogeneous Half-Space

c_{11} (GPa)	c_{12} (GPa)	c_{13} (GPa)	c_{33} (GPa)	c_{44} (GPa)	ρ (g/cm³)
25.5	2.0	14.0	18.4	5.6	2.4

$$f(t) = e^{-0.5f_0^2(t-t_0)^2} \cos \pi f_0(t - t_0), \qquad (27)$$

with $t_0 = 0.5$ s and a high cutoff frequency $f_0 = 10$ Hz, is assumed to be located at the free surface of a 3D half-space (Fig. 5). It should be mentioned that Carcione *et al.* (1992) and Carcione (2000) presented an analytical comparison of the point-source response in a 3D VTI medium in the absence of the free surface. The comparisons are performed by first transforming the 3D numerical results into a line-source response by carrying out an integration along the receiver line (Wapenaar *et al.*, 1992) and then comparing the emerging results with the 2D Lamb's analytical solutions. The numerical model contains $401 \times 401 \times 191$ grid nodes in the *x*, *y*, and *z* directions, respectively. The grid spacings are 10 m in all directions. The solution is advanced using a timestep of 1.25 ms for 3.5 s.

Three receiver lines are positioned on the free surface, two of which are parallel to the *y* direction with respective normal distances of 130 (Line 1) and 1000 m (Line 2) away from the point source, the other crosses the source location and parallels the *x* direction (Line 3). The integrations are performed along the first two receiver lines; these represent 2D results of 130 and 1000 m away from the source, respectively. Figure 6 shows the comparisons between the resulting numerical and 2D analytical *z* components of the displacement for the VTI medium. In spite of the errors resulting from the transformation of the point-source response into the line-source one, numerical and analytical results agree well in Figure 6. These comparisons demonstrate the accuracy of our corresponding algorithm.

Figure 5. Model of a half-space with a planar free surface. The source locates at (300 m, 2000 m) at the surface, which is marked as an asterisk. Three receiver lines (Line 1, Line 2, and Line 3) are also marked. Lines 1 and 2 are parallel to the *y* direction with normal distances of 130 and 1000 m from the point-source, respectively. Line 3 crosses the source location and lies in the *x* direction.

Synthetic seismograms are computed at Line 3. The seismograms in Figure 7 show the direct quasi-*P* wave (*qP*) and a high-amplitude Rayleigh wave (*R*). Snapshots of the vertical component of the wave field in the horizontal (*xy*) plane at the propagation time of 1.4 s are displayed in Figure 8. We define the incidence plane by the propagation direction and the *z* axis, quasi-*P* wave and quasi-*SV* wave (*qSV*) motions lie in this plane, while *SH* motion is normal to the plane. Hence, the *z* component does not contain *SH* motion. The *xy* plane of a transversely isotropic medium is a plane of isotropy, where the velocity of the *qP* wave is about 3260 ms⁻¹ and the velocity of the *qSV* wave is about 1528 ms⁻¹. The amplitude of the *qP* wave is so weak compared with that of the Rayleigh and *qSV* wave that one can

Figure 4. Accuracy of the numerical method for the Lamb's problem in the isotropic medium. The envelope and phase misfits are evaluated against the normalized epicentral distance. Sampling ratios 6 and 12 are used in the numerical solutions, respectively.
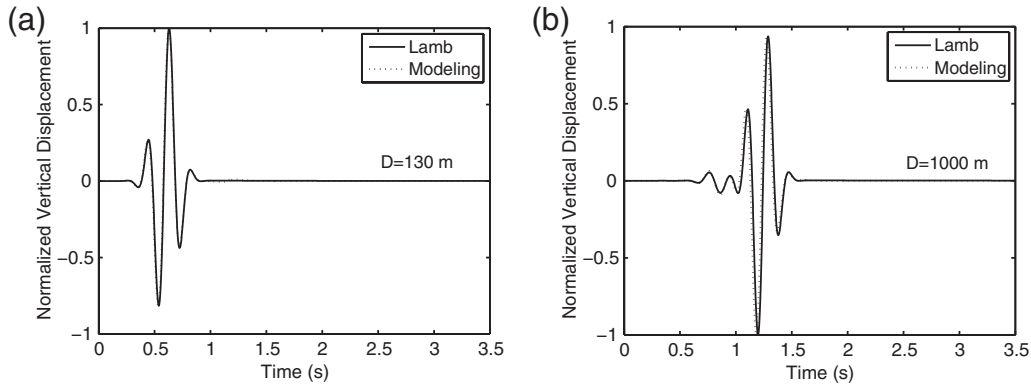
Figure 6. Comparison between numerical and analytical vertical components of the displacement for the Lamb's problem in the VTI medium: (a) Line 1 parallels the *y* direction, at normal distance of 130 m from the energy source (Fig. 5); (b) Line 2 parallels the *y* direction, at normal distance of 1000 m from the energy source. Lamb's result is an analytical solution of the 2D Lamb's problem of the VTI medium. The modeling result is the line-source response of the 3D VTI medium obtained by the superposition of the 3D point-source responses. A good agreement is observed.

hardly identify it in the snapshot (Fig. 8a). In order to observe the *qP* wave, the amplitude of the wave field is amplified 10 times. Owing to this, side reflections also appear in the photo, as shown in Figure 8b. As the velocity of the Rayleigh wave is very close to that of the *qSV* wave, the two waves are almost superimposed, and it is difficult to distinguish between the two in synthetic seismograms and snapshots.

Figure 9 shows the *x*-component of the wave field in the vertical (*xz*) plane at 1.4 and 2.3 s propagation times. The *xz* plane contains the receiver line (Line 3) and the source location. Both snapshots show the wave front of the *qP* wave and the *qSV* wave. The former snapshot (1.4 s) shows the *qSV* wave with the cusps. A headwave (*H*) can also be found in the photos; the headwave is a quasi-shear wave and is guided along the surface by the *qP* wave.

Numerical Simulations on an Irregular (Nonflat) Free Surface

Three numerical experiments with irregular free surfaces are now investigated. The first example is a test on smooth boundaries, while the second example consists of a hemispherical depression to test the ability of the method for nonsmooth topography. For the sake of simplicity, both examples are based on homogeneous half-spaces, that is, the medium parameters are the same as in the case of a flat surface (Table 1). The same source is located at the same place as in the planar surface model, the timestep is 0.8 ms. The total propagation time is 3.5 s for the two models. Finally, we consider a two-layered model with a realistic topography.

Topography Simulating a Shaped Gaussian Hill. The first model considered here is a half-space whose free surface is a hill-like feature (Fig. 10). The shape of the hill resembles a Gaussian curved surface given by the function

$$z(x, y) = -150 \exp\left[-\left(\frac{x - 2000}{150}\right)^2 - \left(\frac{y - 2000}{150}\right)^2\right] \text{ m},$$

$$(x, y) \in [0 \text{ m}, 4000 \text{ m}]^2. \tag{28}$$

The computational domain extends to depth $z(x, y) = 2000$ m. The volume is discretized with equal grid nodes in each direction as in the planar surface one. The grid spacings are 10 m in the *x* and *y* directions and about 10.5 m
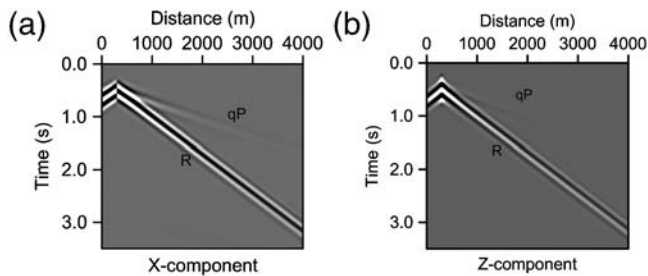
Figure 7. Seismograms along Line 3 that cross the source location and are parallel to the *x* direction (Fig. 5), for the planar surface model: (a) *x*-component (horizontal) of the displacement; (b) *z*-component (vertical). Symbol *qP* indicates the *qP* wave; *R* indicates Rayleigh wave.
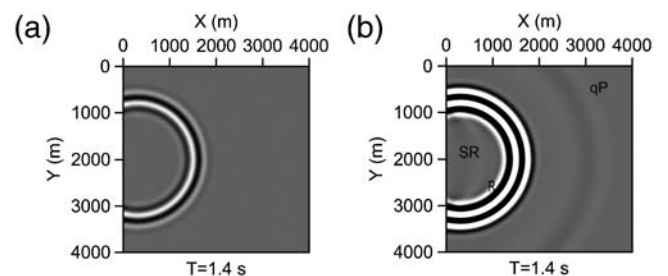

Figure 8. Snapshots of the vertical component of the wave field at the surface (*xy* plane) of the planar surface model. The amplitude of the wave field in (b) is 10 times enlarged compared with (a). The quasi-*P* wave (*qP*), Rayleigh wave (*R*), and side reflections are marked (SR).
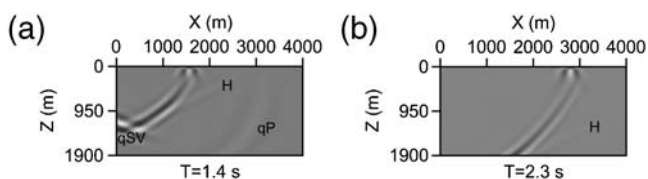
Figure 9. Snapshots of the x component of the wave field in the vertical (xz) plane that contains the receiver line and the source at (a) 1.4 s and (b) 2.3 s propagation times for the planar surface model. The quasi-P wave (qP), quasi-SV wave (qSV), and a head wave (H) generated at the free surface are marked.

in the z direction for average. The vertical spacing varies with depth; it is smaller toward the free surface and larger toward the bottom of the model. The minimum and maximum of the vertical spacings are 6 and 12 m, respectively.

The gridding scheme that shows the detailed cross section of the grids along Line 3 is shown in Figure 11. Synthetic seismograms are also computed at Line 3 (Fig. 12). As a result of the hill-shaped free surface (and compared with the synthetic seismograms in Figure 7), the amplitudes of the quasi-P wave and Rayleigh wave are reduced in the right part of the sections. In addition, after the ordinary quasi-P wave a secondary quasi-P wave ($RqPf$) induced by the scattering of the direct Rayleigh wave can be observed. Similarly, a secondary Rayleigh wave ($qPRf$) that travels in front of the ordinary Rayleigh wave induced by the scattering of the direct quasi-P wave can also be distinguished. Some energy is scattered back to the left side as a Rayleigh wave ($qPRb$, RR) and a quasi-P wave ($RqPb$).

Snapshots of the wave field in the horizontal (xy) plane at different propagation times are displayed in Figure 13. The amplitudes are 10 times enlarged. In the beginning the wave field propagates undisturbed along the free surface. At 1.1 s the direct quasi-P wave hits the hill and generates a circular
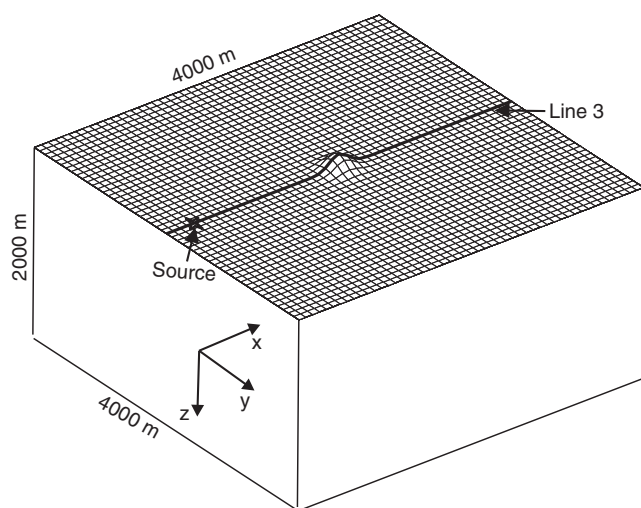
Figure 10. Model of a half-space with Gaussian shape hill topography. The size of the model is 4000 m × 4000 m × 2000 m. The source locates at (300 m, 2000 m) at the surface, which is marked as an asterisk. The receiver line (Line 3) crossing the source location and lying in the x direction is also marked.
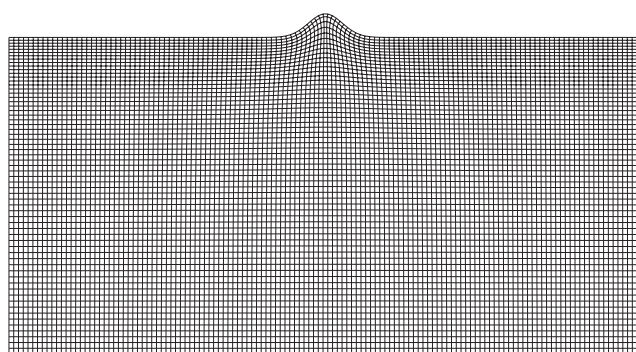
Figure 11. The gridding scheme that shows the detailed cross section of the grids along Line 3 in the Gaussian shape hill topography model. For clarity, the grids are displayed with a reducing density factor of 3.

diffracted wave. This wave is a Rayleigh wave, which is marked as two parts: one travels forward ($qPRf$) and the other travels backward ($qPRb$). These can be seen clearly in the later snapshots (1.4–2.3 s). In addition, a reflected Rayleigh wave (RR) can be observed. The direct quasi-P wave (qP) and Rayleigh wave (R) are also marked in the figure. By the way, side reflections from the boundaries can also be noted in the plane. Figure 14 shows the x component of the wave field in the vertical (xz) plane. The xz plane contains the receiver line and source location. The snapshots show the diffracted quasi-P and quasi-SV waves clearly in the vertical plane.

Topography Simulating a Shaped Hemispherical Depression. In the second model, we consider a hemispherical depression model as illustrated in Figure 15. The first model that we have considered is of smooth topography, that is, with continuous and finite slopes everywhere. However, the shaped hemispherical depression here taken as a reference is a case of extreme topography, such that the vertical-to-horizontal ratio of the depression is very large (1:2) and the slopes of the edges tend to infinity. The hemispherical
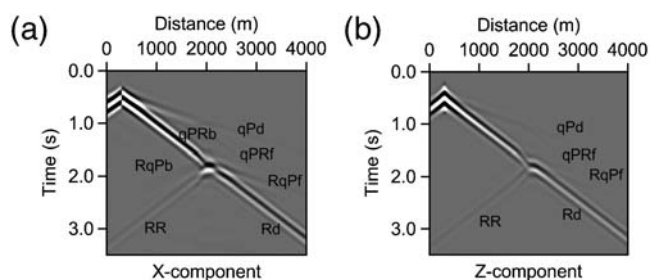

Figure 12. Seismograms along the receiver line for the Gaussian shape hill topography model: (a) x component (horizontal) of the displacement; (b) z component (vertical). Symbols are: qPd: qP wave diffracts to qP wave; Rd: Rayleigh wave diffracts to Rayleigh wave; $qPRf$: qP wave scatters to Rayleigh wave and propagates forward; $qPRb$: qP wave scatters to Rayleigh wave and propagates backward; $RqPf$: Rayleigh wave scatters to qP wave and propagates forward; $RqPb$: Rayleigh wave scatters to qP wave and propagates backward; RR: Rayleigh wave reflects to Rayleigh wave.
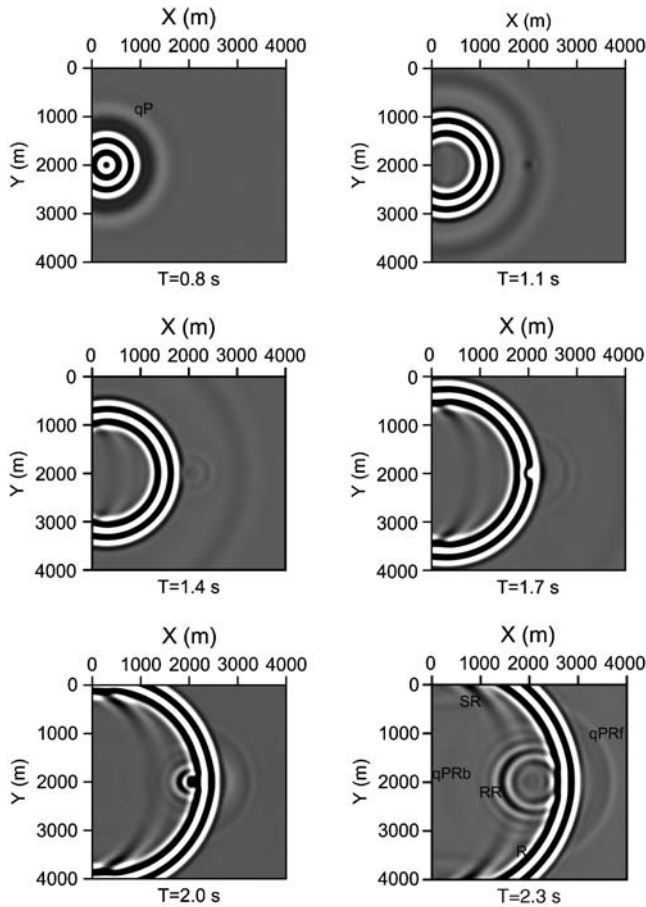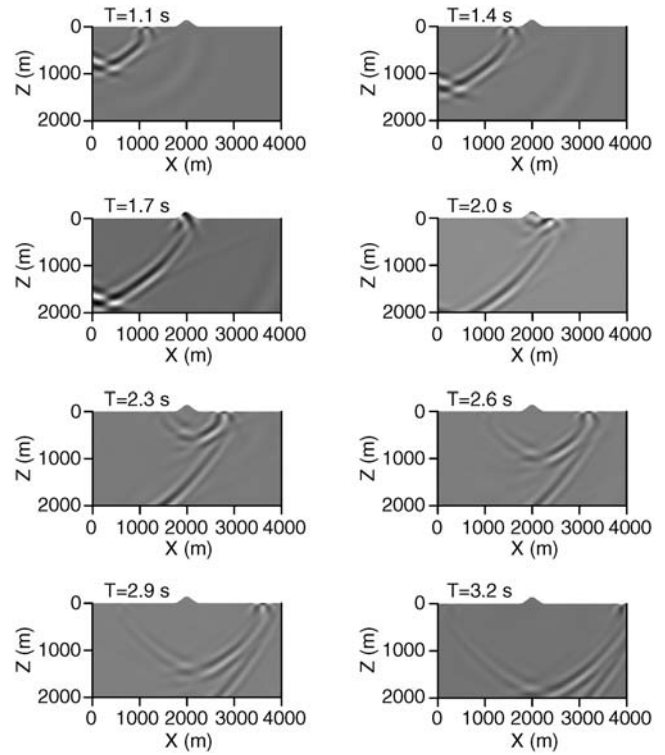
Figure 13. Snapshots of the vertical component of the wave field at the surface (*xy* plane) at different propagation times for the Gaussian shape hill topography model. To see the scattered waves especially the scatterings from the *qP* wave clearly, the amplitudes of the wave field have been amplified 10 times. Side reflections from the boundaries also appear in the photos (SR). Symbols are: *qP*: the *qP* wave; *R*: the Rayleigh wave; *qPRf*: *qP* wave scatters to Rayleigh wave and propagates forward; *qPRb*: *qP* wave scatters to Rayleigh wave and propagates backward; *RR*: Rayleigh wave reflects to Rayleigh wave.

depression is at the middle of the free surface, and the radius is 150 m.

The numerical model is discretized in the same way as in the hill topography model. The gridding scheme that shows the detailed cross section of the grids along Line 3 is shown in Figure 16. Owing to the existence of model edges with strong slopes at $x = 1850$ and $x = 2150$ m along the receiver line, both body waves and Rayleigh waves scattered by sharp changes in the topography can be clearly observed on the synthetic seismograms shown in Figure 17. Owing to its shorter wavelength, the scattering of Rayleigh waves is much stronger than that of the body waves when propagating through the hemispherical depression, thus indicating that such sharp depression can affect the propagation of Rayleigh waves significantly.

The photos in Figure 18 show the vertical component of the wave field in the horizontal (*xy*) plane. Compared with

Figure 14. Snapshots of the *x* component of the wave field in the vertical (*xz*) plane that contains the receiver line and the source at different propagation times for the Gaussian shape hill topography model.

the photos of the hill topography model, we can see the Rayleigh wave scattering at the edges of the hemispherical depression; it seems as if the reflected Rayleigh wave propagates faster in the hemispherical depression model than in the hill topography model. What's more, the back-scattered
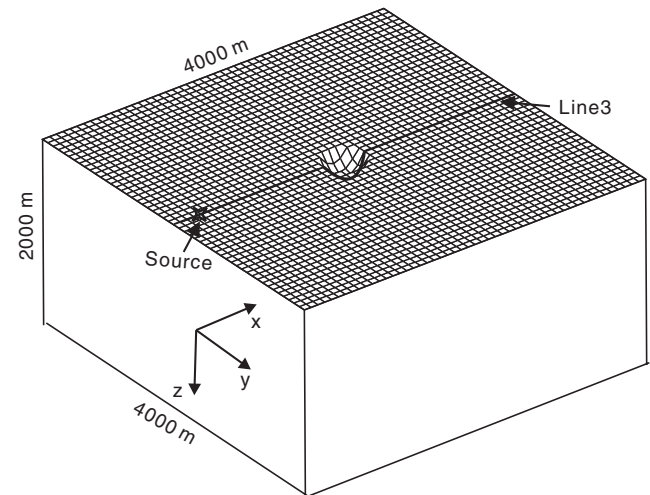
Figure 15. Model of a half-space with hemispherical shape depression topography. The size of the model is 4000 m× 4000 m × 2000 m. The source locates at (300 m, 2000 m) at the surface, which is marked as an asterisk. The receiver line (Line 3) crossing the source location and lying in the *x* direction is also marked.
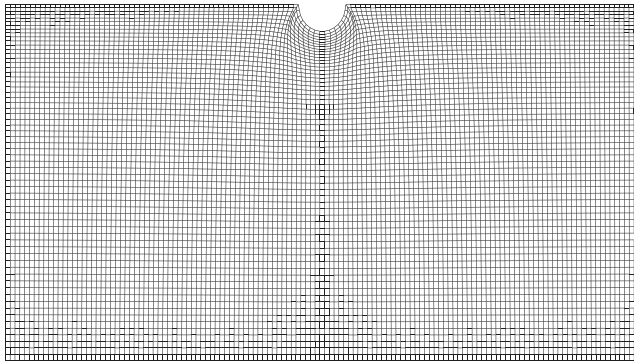
Figure 16. The gridding scheme that shows the detailed cross section of the grids along Line 3 in the hemispherical shape depression topography model. For clarity, the grids are displayed with a reducing density factor of 3.

waves of Rayleigh wave in the hemispherical depression model are much stronger; this may also indicate that such sharp depression blocks the propagation of Rayleigh wave more significantly.

Real Topography Simulating. It is also interesting to study a realistic example. We consider a model in Tibet (Fig. 19). The length and width of the model are 21.6 km, and the average height of the topography is roughly -3560 m (3560 m in the geodetic coordinate system). The digital elevation data set is provided by International Scientific & Technical Data Mirror Site, Computer Network Information Center, Chinese Academy of Sciences (see the Data and Resources section). The computational domain is extended to depth $z(x, y) = 7200$ m. For simplicity we use a two-layered model with parameters given in the model sketch (Fig. 19) instead of the real velocity structure under the realistic topography. It consists of $241 \times 241 \times 121$ grid nodes in the x, y, and z directions, respectively, with equal vertical grid nodes in each layer. A vertical point source such as the one used in previous models is loaded in the middle of the free surface,
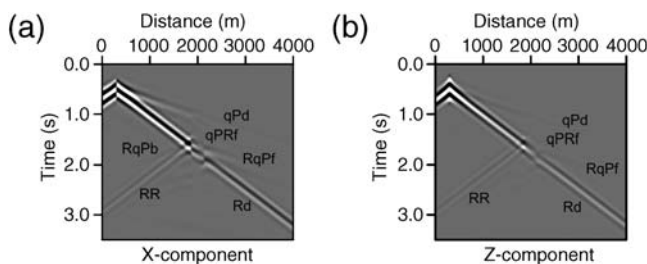
Figure 17. Seismograms at the receiver line for the hemispherical shape depression topography model: (a) x component (horizontal) of the displacement; (b) z component (vertical). Symbols are: qPd: qP wave diffracts to qP wave; Rd: Rayleigh wave diffracts to Rayleigh wave; $qPRf$: qP wave scatters to Rayleigh wave and propagates forward; $qPRb$: qP wave scatters to Rayleigh wave and propagates backward; $RqPf$: Rayleigh wave scatters to qP wave and propagates forward; $RqPb$: Rayleigh wave scatters to qP wave and propagates backward; RR: Rayleigh wave reflects to Rayleigh wave.
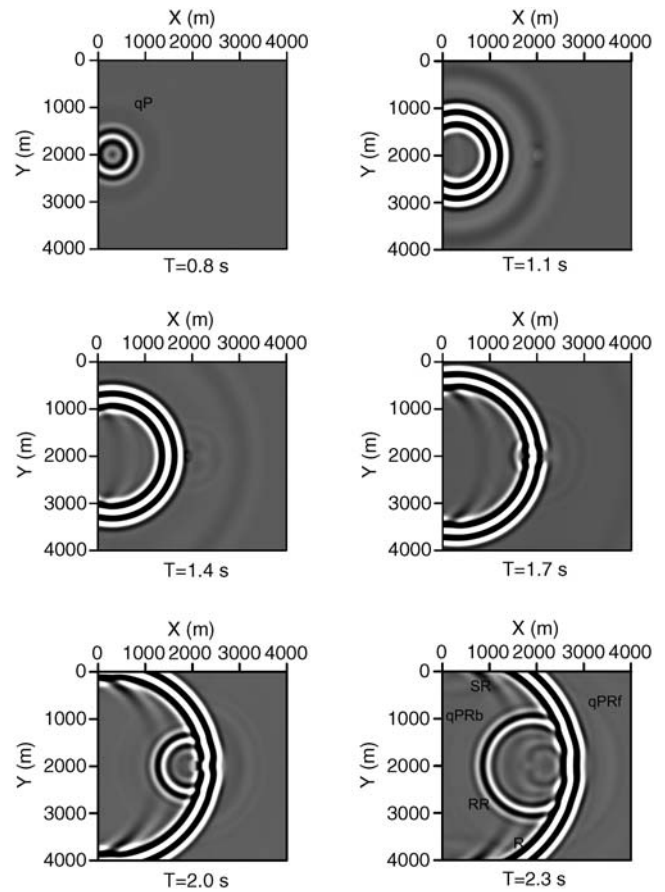

Figure 18. Snapshots of the vertical component of the wave field at the surface (xy plane) at different propagation times for the hemispherical shape depression topography model. To see the scattered waves especially the scatterings from the qP wave clearly, the amplitudes of the wave field have been amplified 10 times. Side reflections from the boundaries also appear in the photos (SR). Symbols are: qP: the qP wave; R: the Rayleigh wave; $qPRf$: qP wave scatters to Rayleigh wave and propagates forward; $qPRb$: qP wave scatters to Rayleigh wave and propagates backward; RR: Rayleigh wave reflects to Rayleigh wave.

where the high cutoff frequency has been changed to 2.7 Hz and the time-shift is 1.5 s. Two lines of receivers crossing the source location and paralleling the x and y directions, respectively, are placed at the free surface. The timestep is 5 ms, and the total propagation time is 8 s.

Snapshots of the z component of the wave field in the vertical plane that contains receiver Line 1 and the source location are presented on Figure 20, and the seismograms of the z component are also computed at the two receiver lines (Fig. 21). We can see that the effect of the topography is very important, with strong scattered phases that are superimposed to the direct and reflected waves, which make it very difficult to identify effective reflections from subsurface interface. The scattering in the seismograms also reflect different features of the surface. The scattering in the seismograms at Line 1 (Fig. 21a) is much stronger than in the seismogram at Line 2 (Fig. 21b), indicating that the surface along Line 1 is much rougher than along Line 2, which also
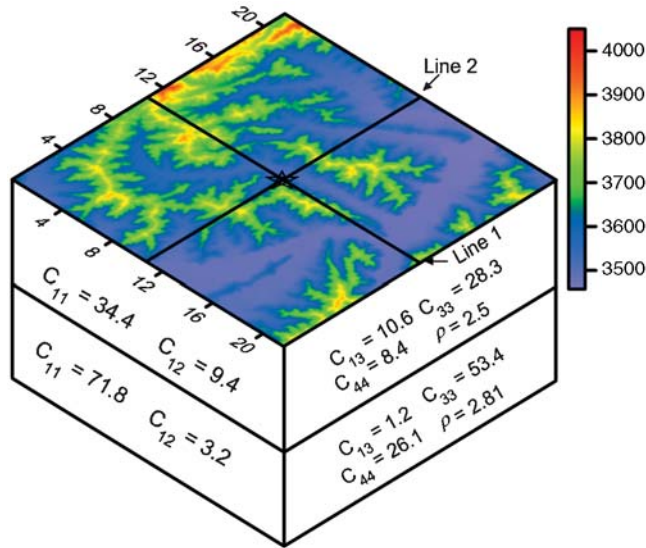
Figure 19. A two-layered model with a realistic topography. The medium parameters of each layer are also given in the figure. The surface shows the topography in a 21.6×21.6 km^2 area in Tibet. Labels are in kilometers and elevations are in meters above mean sea level. The units for the elasticity and density are GPa and g/cm^3, respectively. The location of the source on the surface is indicated by the asterisk. The two receiver lines crossing the source location are also marked.
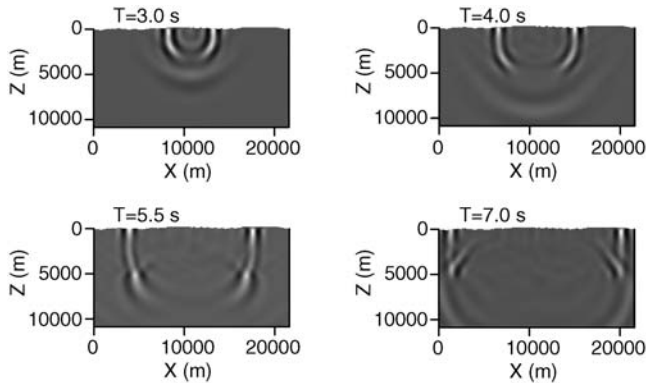

Figure 20. Snapshots of the vertical component of the wave field in the vertical (xz) plane along Line 1 at different propagation times for the two-layered model with a realistic topography.
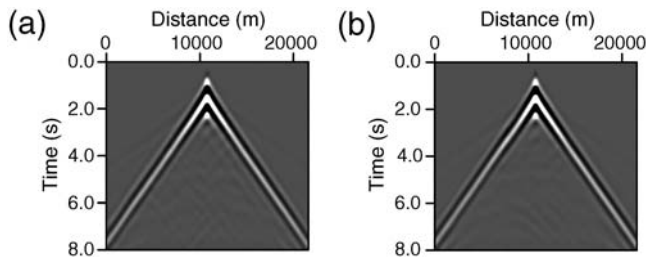
Figure 21. Vertical-component synthetic seismograms coming from the two-layered model with real topography represented in Figure 19: (a) at the receiver line (Line 1) that crosses the source location and is parallel to the x direction (Fig. 19); (b) at the receiver line (Line 2) that crosses the source location and is parallel to the y direction.

can be observed in Figure 19. What's more, the scattering in Figure 21a is almost uniformly distributed, while in Figure 21b it is mostly distributed in the vicinity of the shot. These may due to different distributions of the surface topography along these two lines.

Conclusion

We propose a stable and explicit finite-difference method to simulate with second-order accuracy the propagation of seismic waves in a 3D heterogeneous transversely isotropic medium with nonflat free surface. The method is an extension of the 2D method proposed by Appelo and Petersson (2009) to the 3D anisotropic case. The surface topography is introduced via mapping rectangular grids to curved grids. The accurate application of the free-surface boundary conditions is done by using boundary-modified difference operators to discretize the mixed derivatives in the governing equations of the problem. Several numerical examples under different assumptions of free surface are given to highlight the complications of realistic seismic-wave propagation in the vicinity of the earth surface. Synthetic seismograms and snapshots explain diffractions, scattering, multiple reflections, and converted waves provoked by the features of the free-surface topography. The typical cuspidal triangles of the quasi-transverse (qS) mode also appear in the snapshots of the anisotropic medium.

The future directions of our research will include an extension of the schemes to the viscoelastic case. This will allow a realistic attenuation of the seismic waves due to the presence of a weathered layer to be included (Carcione *et al.*, 1988; Carcione, 1993, 2000).

Data and Resources

Acknowledgments

References

Al-Shukri, H. J., G. L. Pavlis, and F. L. Vernon III(1995). Site effect observations from broadband arrays, *Bull. Seismol. Soc. Am.* **85,** 1758–1769.

Appelo, D., and N. A. Petersson (2009). A stable finite difference method for the elastic wave equation on complex geometries with free surfaces, *Commun. Comput. Phys.* **5,** 84–107.

Ashford, S. A., N. Sitar, J. Lysmer, and N. Deng (1997). Topographic effects on the seismic response of steep slopes, *Bull. Seismol. Soc. Am.* **87,** 701–709.

Backus, G. E. (1962). Long-wave elastic anisotropy produced by horizontal layering, *J. Geophys. Res.* **67,** 4427–4440.

Boore, D. M. (1972). A note on the effect of simple topography on seismic *SH* waves, *Bull. Seismol. Soc. Am.* **62,** 275–284.

Bouchon, M., M. Campillo, and S. Gaffet (1989). A boundary integral equation-discrete wavenumber representation method to study wave propagation in multilayered medium having irregular interfaces, *Geophysics* **54,** 1134–1140.

Bouchon, M., C. A. Schultz, and M. N. Toksoz (1995). A fast implementation of boundary integral equation methods to calculate the propagation of seismic waves in laterally varying layered medium, *Bull. Seismol. Soc. Am.* **85,** 1679–1687.

Campillo, M. (1987). Modeling of *SH* wave propagation in an irregularly layered medium. Application to seismic profiles near a dome, *Geophys. Prospecting* **35,** 236–249.

Campillo, M., and M. Bouchon (1985). Synthetic *SH* seismograms in a laterally varying medium by the discrete wavenumber method, *Geophys. J. R. Astr. Soc.* **83,** 307–317.

Carcione, J. M. (1993). Seismic modeling in viscoelastic medium, *Geophysics* **58,** 110–120.

Carcione, J. M. (2000). *Wave Fields in Real Medium: Wave Propagation in Anisotropic, Anelastic and Porous Medium*, Pergamon, Amsterdam.

Carcione, J. M., D. Kosloff, A. Behle, and G. Seriani (1992). A spectral scheme for wave propagation simulation in 3-D elastic-anisotropic medium, *Geophysics* **57,** 1593–1607.

Carcione, J. M., D. Kosloff, and R. Kosloff (1988). Viscoacoustic wave propagation simulation in the earth, *Geophysics* **53,** 769–777.

Cerjan, C., D. Kosloff, R. Kosloff, and M. Reshef (1985). A nonreflecting boundary condition for discrete acoustic and elastic wave equations, *Geophysics* **50,** 705–708.

Crampin, S. (1981). A review of wave motion in anisotropic and cracked elastic-medium, *Wave Motion* **3,** 343–391.

Crampin, S. (1984). Effective anisotropic elastic constants for wave propagation through cracked solids, *Geophys. J. Int.* **76,** 135–145.

Durand, S., S. Gaffet, and J. Virieux (1999). Seismic diffracted waves from topography using 3-D discrete wavenumber-boundary integral equation simulation, *Geophysics* **64,** 572–578.

Dziewonski, A. M., and D. L. Anderson (1981). Preliminary reference Earth model, *Phys. Earth Planet. In.* **25,** 297–356.

Fornberg, B. (1988). The pseudo-spectral method: Accurate representation in elastic wave calculations, *Geophysics* **53,** 625–637.

Forsyth, D. W. (1975). The early structural evolution and anisotropy of the oceanic upper mantle, *Geophys. J. Int.* **43,** 103–162.

Frankel, A. (1993). Three-dimensional simulations of ground motion in the San Bernardino Valley, California, for hypothetical earthquakes on the San Andreas fault, *Bull. Seismol. Soc. Am.* **83,** 1020–1041.

Frankel, A., and J. Vidale (1992). A three-dimensional simulation of seismic waves in the Santa Clara Valley, California, from a Loma Prieta aftershock, *Bull. Seismol. Soc. Am.* **82,** 2045–2074.

Galis, M., P. Moczo, and J. Kristek (2008). A 3-D hybrid finite-difference—Finite-element viscoelastic modelling of seismic wave motion, *Geophys. J. Int.* **175,** 153–184.

Gao, H., and J. Zhang (2006). Parallel 3-D simulation of seismic wave propagation in heterogeneous anisotropic medium: A grid method approach, *Geophys. J. Int.* **165,** 875–888.

Grechka, V. Y., and G. A. McMechan (1995). Is shear-wave splitting an indicator of seismic anisotropy?, *SEG Expanded Abstracts* **14,** 332–335.

Hayashi, K., D. R. Burns, and M. N. Toksoz (2001). Discontinuous-grid finite-difference seismic modeling including surface topography, *Bull. Seismol. Soc. Am.* **91,** 1750–1764.

He, Q., and Z. Zhang (1996). *Seismic Propagation and Numerical Simulation in Transversely Isotropic Medium*, Jilin University Press (in Chinese).

Helbig, K. (1984). Anisotropy and dispersion in periodically layered medium, *Geophysics* **49,** 364–373.

Hestholm, S. (2003). Elastic wave modeling with free surfaces: Stability of long simulations, *Geophysics* **68,** 314–321.

Hestholm, S., and B. Ruud (1994). 2-D finite-difference elastic wave modeling including surface topography, *Geophys. Prosp.* **42,** 371–390.

Hestholm, S., and B. Ruud (1998). 3-D finite-difference elastic wave modeling including surface topography, *Geophysics* **63,** 613–622.

Hestholm, S. O., B. O. Ruud, and E. S. Husebye (1999). 3-D versus 2-D finite-difference seismic synthetics including real surface topography, *Phys. Earth Planet. Inter.* **113,** 339–354.

Hsu, C. J., and M. Schoenberg (1993). Elastic waves through a simulated fractured medium, *Geophysics* **58,** 964–977.

Hudson, J. A. (1981). Wave speeds and attenuation of elastic waves in material containing cracks, *Geophys. J. Int.* **64,** 133–150.

Hvid, S. L. (1994). Three dimensional algebraic grid generation, *Ph.D. Thesis*, Technical University of Denmark.

Jih, R. S., K. L. McLaughlin, and Z. A. Der (1988). Free-boundary conditions of arbitrary polygonal topography in a two-dimensional explicit elastic finite-difference scheme, *Geophysics* **53,** 1045.

Komatitsch, D., and J. Tromp (1999). Introduction to the spectral element method for three-dimensional seismic wave propagation, *Geophys. J. Int.* **139,** 806–822.

Komatitsch, D., and J. Tromp (2002). Spectral-element simulations of global seismic wave propagation-I. Validation, *Geophys. J. Int.* **149,** 390–412.

Komatitsch, D., and J. P. Vilotte (1998). The spectral element method: an efficient tool to simulate the seismic response of 2D and 3D geological structures, *Bull. Seismol. Soc. Am.* **88,** 368–392.

Kristek, J., P. Moczo, and R. J. Archuleta (2002). Efficient methods to simulate planar free surface in the 3D fourth-order staggered-grid finite-difference schemes, *Studia Geophys. Geod.* **46,** no. 2, 355–381.

Levander, A. R. (1990). Seismic scattering near the earth's surface, *Pure Appl. Geophys.* **132,** 21–47.

Liu, E., and Z. Zhang (2001). Numerical study of elastic wave scattering by cracks or inclusions using the boundary integral equation method, *J. Comput. Acoust.* **9,** 1039–1054.

Liu, E., S. Crampin, J. H. Queen, and W. D. Rizer (1993). Velocity and attenuation anisotropy caused by microcracks and microfractures in a multiazimuth reverse VSP, *Can. J. Explor. Geophys.* **29,** 177–188.

Liu, E., Z. Zhang, J. Yue, and A. Dobson (2008). Boundary integral modelling of elastic wave propagation in multi-layered 2D medium with irregular interfaces, *Commun. Comput. Phys.* **3,** no. 1, 52–62.

Lombard, B., J. Piraux, C. Gélis, and J. Virieux (2008). Free and smooth boundaries in 2-D finite-difference schemes for transient elastic waves, *Geophys. J. Int.* **172,** 252–261.

Moczo, P., E. Bystricky, J. Kristek, J. Carcione, and M. Bouchon (1997). Hybrid modelling of *P-SV* seismic motion at inhomogeneous viscoelastic topographic structures, *Bull. Seismol. Soc. Am.* **87,** 1305–1323.

Nielsen, P., F. If, P. Berg, and O. Skovgaard (1994). Using the pseudospectral technique on curved grids for 2D acoustic forward modelling, *Geophys. Prospect.* **42,** 321–342.

Nilsson, S., N. A. Petersson, B. Sjogreen, and H. O. Kreiss (2007). Stable difference approximations for the elastic wave equation in second order formulation, *SIAM J. Numer. Anal.* **45,** 1902–1936.

Oprsal, I., and J. Zahradník (1999). Elastic finite-difference method for irregular grids, *Geophysics* **64,** 240–250.

Payton, R. G. (1983). *Elastic Wave Propagation in Transversely Isotropic Medium*, Martinus Nijhoff Publishers.

Rial, J. A., N. G. Saltzman, and H. Ling (1992). Earthquake-induced resonance in sedimentary basins, *American Scientist* **80,** 566–578.

Robertsson, J. O. A. (1996). A numerical free-surface condition for elastic/viscoelastic finite-difference modeling in the presence of topography, *Geophysics* **61,** 1921–1934.

Robertsson, J. O. A., and K. Holliger (1997). Modeling of seismic wave propagation near the earth's surface, *Phys. Earth Planet. Inter.* **104,** 193–211.

Sánchez-Sesma, F. J., and M. Campillo (1991). Diffraction of *P*, *SV*, and Rayleigh waves by topographic features: A boundary integral formulation, *Bull. Seismol. Soc. Am.* **81,** 2234–2253.

Sánchez-Sesma, F. J., and M. Campillo (1993). Topographic effects for incident *P*, *SV* and Rayleigh waves, *Tectonophysics* **218,** 113–125.

Sánchez-Sesma, F. J., M. A. Bravo, and I. Herrera (1985). Surface motion of topographical irregularities for incident *P*, *SV*, and Rayleigh waves, *Bull. Seismol. Soc. Am.* **75,** 263–269.

Sánchez-Sesma, F. J., J. Ramos-Martínez, and M. Campillo (1993). An indirect boundary element method applied to simulate the seismic response of alluvial valleys for incident *P*, *S* and Rayleigh waves, *Earthquake Eng. Struct. Dynam.* **22,** 279–295.

Schoenberg, M., and F. Muir (1989). A calculus for finely layered anisotropic medium, *Geophysics* **54,** 581–589.

Tessmer, E., and D. Kosloff (1994). 3-D elastic modeling with surface topography by a Chebychev spectral method, *Geophysics* **59,** 464–473.

Tessmer, E., D. Kosloff, and A. Behle (1992). Elastic wave propagation simulation in the presence of surface topography, *Geophys. J. Int.* **108,** 621–632.

Thompson, J. F., Z. U. A. Warsi, and C. W. Mastin (1985). *Numerical Grid Generation: Foundations and Applications*, North-holland, Amsterdam.

Toshinawa, T., and T. Ohmachi (1992). Love wave propagation in a three-dimensional sedimentary basin, *Bull. Seismol. Soc. Am.* **82,** 1661–1667.

Wapenaar, C., D. Verschuur, and P. Herrmann (1992). Amplitude preprocessing of single and multicomponent seismic data, *Geophysics* **57,** 1178–1188.

Wong, H. L. (1982). Effect of surface topography on the diffraction of *P*, *SV*, and Rayleigh waves, *Bull. Seismol. Soc. Am.* **72,** 1167–1183.

Yang, D. (1996). Forward simulation and inversion of seismic wave equations in anisotropic medium, *Ph.D. Dissertation*, Institute of Geophysics, Chinese Academy of Sciences.

Yang, D. H., E. Liu, Z. J. Zhang, and J. Teng (2002). Finite-difference modelling in two-dimensional anisotropic medium using a flux-corrected transport technique, *Geophys. J. Int.* **148,** 320–328.

Yang, D., S. Wang, Z. Zhang, and J. Teng (2003). *n*-Times absorbing boundary conditions for compact finite-difference modeling of acoustic and elastic wave propagation in the 2D TI medium, *Bull. Seismol. Soc. Am.* **93,** 2389–2401.

Zhang, H., and X. Chen (2006). Dynamic rupture on a planar fault in three-dimensional half-space—I. Theory, *Geophys. J. Int.* **164,** no. 3, 633–652.

Zhang, W., and X. Chen (2006). Traction image method for irregular free surface boundaries in finite difference seismic wave simulation, *Geophys. J. Int.* **167,** 337–353.

Zhang, Z., and S. L. Klemperer (2010). Crustal structure of the Tethyan Himalaya, south Tibet: New constraints from old wide-angle seismic data, *Geophys. J. Int.* **181,** 1247–1260.

Zhang, Z., Q. He, and Z. Xu (1993). Absorbing boundary condition for FD modeling in 2D inhomogeneous TIM, *Chin. J. Geophys.* **36,** no. 6, 519–527.

Zhang, Z., J. Teng, and Z. He (2000). Azimuthal anisotropy of seismic velocity, attenuation and *Q* value in viscous EDA medium, *Sci. China E* **43,** 17–22.

Zhang, Z., G. Wang, and J. M. Harris (1999). Multi-component wavefield simulation in viscous extensively dilatancy anisotropic medium, *Phys. Earth Planet. Inter.* **114,** 25–38.

Zhang, Z., X. Yuan, Y. Chen, X. Tian, R. Kind, X. Li, and J. Teng (2010). Seismic signature of the collision between the east Tibetan escape flow and the Sichuan Basin, *Earth Planet Sci Lett.* **292,** 254–264.

Appendix A

Partial Derivatives and Jacobian

In the Transformation between Curvilinear and Cartesian Coordinates section, the formulation involves the partial derivatives $\partial q/\partial x$, $\partial q/\partial y$, $\partial q/\partial z$, $\partial r/\partial x$, $\partial r/\partial y$, $\partial r/\partial z$, $\partial s/\partial x$, $\partial s/\partial y$, $\partial s/\partial z$. They can be found from

$$\mathbf{a^i} = \nabla \xi^i = \frac{1}{J}(\mathbf{a_j} \times \mathbf{a_k}), \qquad (i = 1, 2, 3), \tag{A1}$$
$$(i, j, k)\text{cyclic},$$

where $\mathbf{a^i}$ ($i = 1, 2, 3$) are the three contravariant base vectors of the curvilinear coordinate system, where the three curvilinear coordinates are represented by ξ^i ($i = 1, 2, 3$), that is, q, r, and s in this paper. The contravariant base vectors are normal to the three coordinate surfaces. $\mathbf{a_i}$ ($i = 1, 2, 3$) are the three covariant base vectors of the curvilinear coordinate system, and the subscript i in $\mathbf{a_i}$ indicates the base vector corresponding to the ξ^i coordinate, that is, the tangent to the coordinate line along which only ξ^i varies. The covariant base vectors can be expressed in the form

$$\mathbf{a_i} = x_{\xi^i}\mathbf{i} + y_{\xi^i}\mathbf{j} + z_{\xi^i}\mathbf{k}, \qquad (i = 1, 2, 3), \tag{A2}$$

that is,

$$\mathbf{a_1} = x_q\mathbf{i} + y_q\mathbf{j} + z_q\mathbf{k}, \tag{A3}$$

$$\mathbf{a_2} = x_r\mathbf{i} + y_r\mathbf{j} + z_r, \tag{A4}$$

$$\mathbf{a_3} = x_s\mathbf{i} + y_s\mathbf{j} + z_s\mathbf{k}, \tag{A5}$$

where $\mathbf{i}$, $\mathbf{j}$, and $\mathbf{k}$ are unit vectors in the x, y, and z directions, respectively. J is the Jacobian of the transformation and is given by

$$J = \begin{vmatrix} x_q & x_r & x_s \\ y_q & y_r & y_s \\ z_q & z_r & z_s \end{vmatrix}. \tag{A6}$$

Equation (A1) can be written in a more explicit form

$$\mathbf{a^1} = \nabla q = q_x\mathbf{i} + q_y\mathbf{j} + q_z\mathbf{k} = \frac{1}{J}\mathbf{a_2} \times \mathbf{a_3}, \tag{A7}$$

$$\mathbf{a^2} = \nabla r = r_x\mathbf{i} + r_y\mathbf{j} + r_z\mathbf{k} = \frac{1}{J}\mathbf{a_3} \times \mathbf{a_1}, \tag{A8}$$

$$\mathbf{a^3} = \nabla s = s_x \mathbf{i} + s_y \mathbf{j} + s_z \mathbf{k} = \frac{1}{J} \mathbf{a_1} \times \mathbf{a_2}. \qquad (A9)$$

After using equations (A3)–(A5) to substitute the covariant base vectors in equations (A7)–(A9), we can get the expression (4).

Appendix B

Conservative Form of the Momentum Equations

For 3D inhomogeneous, linear, anisotropic elastic medium, the tensor form of the second-order partial differential displacement-stress equations consist of the momentum conservation equation

$$\rho \frac{\partial^2 \mathbf{u}}{\partial t^2} = \nabla \cdot \sigma, \qquad (B1)$$

and the generalized Hook's Law

$$\sigma_{kl} = c_{ijkl} \varepsilon_{ij}, \qquad (B2)$$

where i, j, k, $l = x$, y, z. In curvilinear coordinates, the operator $\nabla \cdot A$ can be expressed in two forms (Thompson *et al.*, 1985), namely: the conservative form

$$\nabla \cdot \mathbf{A} = \frac{1}{J} \sum_{i=1}^{3} [J \mathbf{a^i} \cdot \mathbf{A}]_{\xi^i}, \qquad (B3)$$

and the nonconservative form

$$\nabla \cdot \mathbf{A} = \sum_{i=1}^{3} \mathbf{a^i} \cdot \mathbf{A}_{\xi^i}, \qquad (B4)$$

where $\xi^i \in \{q, r, s\}$, J is the Jacobian of the transformation, and $\mathbf{a^i}$ ($i = 1, 2, 3$) are the contravariant base vectors, which can be found in Appendix A. Substituting the conservative form of the operator ∇ into the momentum conservation equation (5a)–(5c), we can deduce the conservative form of the momentum equation in curvilinear coordinates as equations (7)–(9).

State Key Laboratory of Lithosphere Evolution
Institute of Geology and Geophysics
Chinese Academy of Sciences
Beijing, 100029, PR China
lanhq@mail.iggcas.ac.cn